

Supplementary Materials for
**Electronic structure orientation as a map of in-plane antiferroelectricity
in β' -In₂Se₃**

Joseph L. Spellberg *et al.*

Corresponding author: Sarah B. King, sbking@uchicago.edu

Sci. Adv. **10**, eado2136 (2024)
DOI: 10.1126/sciadv.ado2136

The PDF file includes:

Supplementary Text
Figs. S1 to S19
Table S1
Legend for movie S1
References

Other Supplementary Material for this manuscript includes the following:

Movie S1

Supplementary Text

Photoemission Electron Microscopy (PEEM)

In polarization-dependent PEEM (PD-PEEM), the polarization of linearly-polarized laser illumination is rotated in the sample plane. The illumination is the second harmonic of an optical parametric chirped pulse amplifier (Class 5 Photonics), a home-built nonlinear optical parametric amplifier, or a 1035 nm fundamental (Coherent Monaco). The 2.40 eV excitation ($\lambda = 516$ nm; FWHM = 3 nm) has a pulse duration of about 170 fs and an approximate fluence of $40 \mu\text{J}/\text{cm}^2$. The 3.06 eV excitation ($\lambda = 405$ nm; FWHM = 10 nm) has a pulse duration of about 50 fs and an approximate fluence of $20 \mu\text{J}/\text{cm}^2$. The linearly polarized laser pulses are directed through an appropriate linear polarizer or thin-film polarizing beamsplitter (Eksma) and a zero-order $\lambda/2$ waveplate (Eksma), then into the ultrahigh vacuum chamber (Scienta Omicron) and microscope column (Focus GmbH). The laser illumination is reflected off a near-normal incidence Rh mirror and impinges on the sample with an incidence of 4° such that the rotation of the polarization with the $\lambda/2$ waveplate results in the rotation of the laser polarization effectively in the sample plane. PEEM images are acquired for 10 s at each polarization angle θ_E . The polarization-dependent reflectivity of the Rh mirror, which results in the modulation of the incident laser fluence and thereby a power-dependent modulation of the photoemission intensity, is corrected with previously published methods (32,33). For each excitation energy, we report a 2 to 3-photon photoemission process, as confirmed by a power series in Figure S11.

In contrast to previous work, where the reflectivity of the Rh mirror is quantitatively determined by a second reference sample (32), we integrate across the entire field of view of the β' - In_2Se_3 sample and use the absence of net polarization-dependent absorption to determine the total photoelectrons emitted from the sample as a function of laser polarization, which precisely describes the polarization-dependent reflectivity of the Rh mirror when there is an equal number of each domain orientation. In the regime where the material's polarization response is small, as is the case for β' - In_2Se_3 , this remains a good approximation for the Rh mirror polarization response even when there is an unequal number of each domain. Each image is normalized by the total photoelectron count at a particular θ_E to correct for the polarization dependent reflectivity of the Rh mirror and determine each domain's transition dipole moment, θ_{TDM} . The laser polarization angle at which the total photoelectron count is maximized is taken to be s-polarized with respect to the Rh mirror (45), which corresponds to the vertical axis of the PEEM image. The integrated intensity of each PEEM image before correcting for the Rh reflectivity is plotted with respect to $\lambda/2$ waveplate position and fit to the equation

$$I_{PE}(\theta_E) = A \cos^2(\theta_E - \delta) + C \quad (\text{S1})$$

where δ is the waveplate position that corresponds to s-polarized light. This equation is the same functional form as Equation 1 in the main text, but here is being used to calibrate the laser polarization rather than to measure transition dipole moment directions. The data is then corrected for the Rh reflectivity by dividing each image by its total integrated intensity. To improve signal to noise, difference images are calculated where each image is subtracted from the image taken with orthogonal laser polarization, and spatially binned in 2×2 neighborhoods to create a new image stack. Each pixel of this new stack is fit according to Equation 1, where the phase shift now represents the direction of each domain's transition dipole moment, θ_{TDM} . For the energy dependent experiments shown in Figure 4 in the main text, two different waveplates were used and therefore the initial position of the $\lambda/2$ waveplate was different. The Rh

reflectivity calibration of the orientation of s-polarized light was done using a graphene sample where there is no polarization-dependent photoemission. For the experiment at $h\nu = 2.40$ eV, s-polarized light corresponded to a waveplate position of 43° and for $h\nu = 3.06$ eV it was 138° . Applying this correction to the data results in the offset horizontal axes in Figure 4. To decrease computational time, pixel-by-pixel fitting for the identification of the transition dipole moment orientation was done using Equation S2.

$$I_{PE}(\theta_E) = k_1 + k_2 \cos(2\theta_E) + k_3 \sin(2\theta_E) \quad (\text{S2})$$

This equation is analytically equivalent to Equation S1 where $A = \pm 2\sqrt{k_2^2 + k_3^2}$, $\delta = \frac{1}{2} \tan^{-1}\left(\frac{k_3}{k_2}\right)$, and $C = k_1 \mp \sqrt{k_2^2 + k_3^2}$.

DFT Calculations

For an optical transition from an electronic state i to another state f , the electronic transition dipole moment is given by $\mathbf{D} = \langle f | \nabla | i \rangle$, where the electronic wavefunctions $|i\rangle$ and $|f\rangle$, and \mathbf{D} can be obtained by first-principles DFT calculations through the VASP package (42). It is typically a complex vector and can be defined as

$$\mathbf{D} = \begin{pmatrix} D_x \\ D_y \\ D_z \end{pmatrix} = \begin{pmatrix} |D_x| e^{i\phi_x} \\ |D_y| e^{i\phi_y} \\ |D_z| e^{i\phi_z} \end{pmatrix}.$$

When the electron-photon interaction is treated within the dipole approximation, the optical transition matrix element is proportional to $\mathbf{P} \cdot \mathbf{D}$, where \mathbf{P} is the electric polarization vector of the light and defined as

$$\mathbf{P} = (\cos \theta, \sin \theta, 0).$$

The optical absorption intensity is then given by

$$I \propto |\mathbf{P} \cdot \mathbf{D}|^2.$$

To obtain a nonzero intensity, \mathbf{D} should have a component parallel to the light polarization vector \mathbf{P} , which is an important selection rule for the optical transition (32,46). To understand the experimentally observed wavelength-dependent optical properties, we carried out first-principles simulations of monolayer β' -In₂Se₃ that has the antiferroelectric lattice geometry determined from experiment (20). DFT calculations according to the atomic structure and computational parameters discussed in the Methods section were used to calculate the frequency dependent dielectric function and optical transition matrix of a supercell of β' -In₂Se₃. From these values we calculate the transition dipole moment for specific photoexcitation and photoemission laser-polarization angles. Based on the transition dipole moments, we can calculate the linear dichroism and angle of maximum absorption for a range of excitation energies. For a certain excitation energy, we considered all possible transitions between the valence bands and conduction bands in the BZ that satisfy the energy conservation relation:

$$|\varepsilon_{c\mathbf{k}} - \varepsilon_{v\mathbf{k}} - \omega| \leq 0.1 \text{ eV},$$

where $\varepsilon_{c\mathbf{k}}$ ($\varepsilon_{v\mathbf{k}}$) indicates the energy of a conduction (valence) band state at the \mathbf{k} -point \mathbf{k} , ω corresponds to the incoming photon energy, and 0.1 eV represents the δ function. For an excitation energy, there are many possible transitions that can satisfy the conservation of energy. We computed the averaged angle-dependent absorption intensity by considering contributions from all the transitions, following the formula

$$\bar{I}(\theta) = \frac{\sum_{i=1}^N I_i(\theta) W_i}{\sum_{i=1}^N W_i} \quad (\text{S3})$$

where N is the total number of transitions, $I_i(\theta)$ is the intensity of transition i at the polarization angle of θ , and W_i represents the weight of transition i (set as 1 for equal contribution here). The linear dichroism is then calculated according to

$$\rho(\theta) = \frac{\bar{I}(\theta)_{\max} - \bar{I}(\theta)_{\min}}{\bar{I}(\theta)_{\max} + \bar{I}(\theta)_{\min}} \quad (\text{S4})$$

It is interesting to note that among all transitions, only transitions with the dipole moments parallel or perpendicular to the nanostripe direction (or the electric polarization direction) have notable intensities, and thus the angle of maximum absorption for the averaged intensity corresponds to the direction either parallel or perpendicular to the electric polarization regardless of the excitation energy, as discussed in the main text. This highlights the strong correlation between the transition dipole moment and the electric polarization in β' -In₂Se₃.

Sample Preparation and Data Analysis

β' -In₂Se₃ flakes were produced by mechanical exfoliation of bulk α -In₂Se₃ followed by annealing on a hot plate in N₂ atmosphere. Flakes were confirmed to be in the β' phase by cross polarized optical microscopy and Raman spectroscopy, Figures S1-2. Atomic force microscopy was used to measure flake thicknesses and to confirm that flake surfaces were flake within nanometer precision, Figure S4.

Image resolution was determined by measuring the θ_{TDM} value at each pixel along a series of line cuts that span domain boundaries, Figures S8-9. Difference PE intensity values images were also plotted along the same linecuts as well as the R^2 of each pixel along the fit. Ultimate resolution is dependent on the field of view of the image, but sub-100 nm resolution is attainable for a field of view of 20 μm with the best resolution seen was ~ 50 nm.

Geometric Analysis of AFE Domain Shapes

The geometric rules describing domain boundary formation in β' -In₂Se₃ were derived from atomic-scale STEM imaging by Xu *et al.* (7). There are three directions that nanostripes can point: along any of the symmetry equivalent $[\bar{1}120]$ lattice vectors. Domain boundaries can form along the $[\bar{1}120]$ lattice vectors or along the three $[\bar{1}100]$ directions. $[\bar{1}120]$ and $[\bar{1}100]$ vectors are perpendicular with each other. There are therefore six possible boundary orientations, shown schematically in Figure S15(a). With only these six orientations available, the interior angles of domains will always be multiples of 30°. Nanostripes will form a symmetric angle about the boundary which will either be 60° or 120°. Asymmetric boundaries are ‘forbidden’ according to

these rules, so domains will never be enclosed by a boundary that is parallel or perpendicular to its nanostripes.

When enclosing a domain with boundaries all from the same set of lattice vectors, the simplest shape that can be formed is a 60-120 parallelogram. If it is bound by $[11\bar{2}0]$ vectors, the nanostripes will point along the domain's minor axis and if it is bound by $[1\bar{1}00]$ vectors the nanostripes will point along the major axis (Figure S16(a)). Without knowledge of the crystalline axes, however, the nanostripe directions cannot be determined from the domain shape, only that they must point in one of two directions (Figure S16(b)).

When domain shapes are constructed using boundaries from both sets of vectors, other shapes are possible, as shown in Figure S17(a). The interior angles will always be a multiple of 30° . If the lattice vectors are unknown, boundary shapes will still have two possible nanostripe orientations. A 30-60-90 triangle is included as an example. Rectangles are a unique case because they only include a single boundary from each vector set so there are four possible orientations that the nanostripes can point (Figure S17(b)).

From these constraints on individual domain shapes, we can extend the analysis to multidomain patterns to predict how AFE domains can arrange in β' - In_2Se_3 . The geometric expectations derived from the atomic scale are also valid for the domains observed via electronic structure in PD-PEEM (Figure S18).

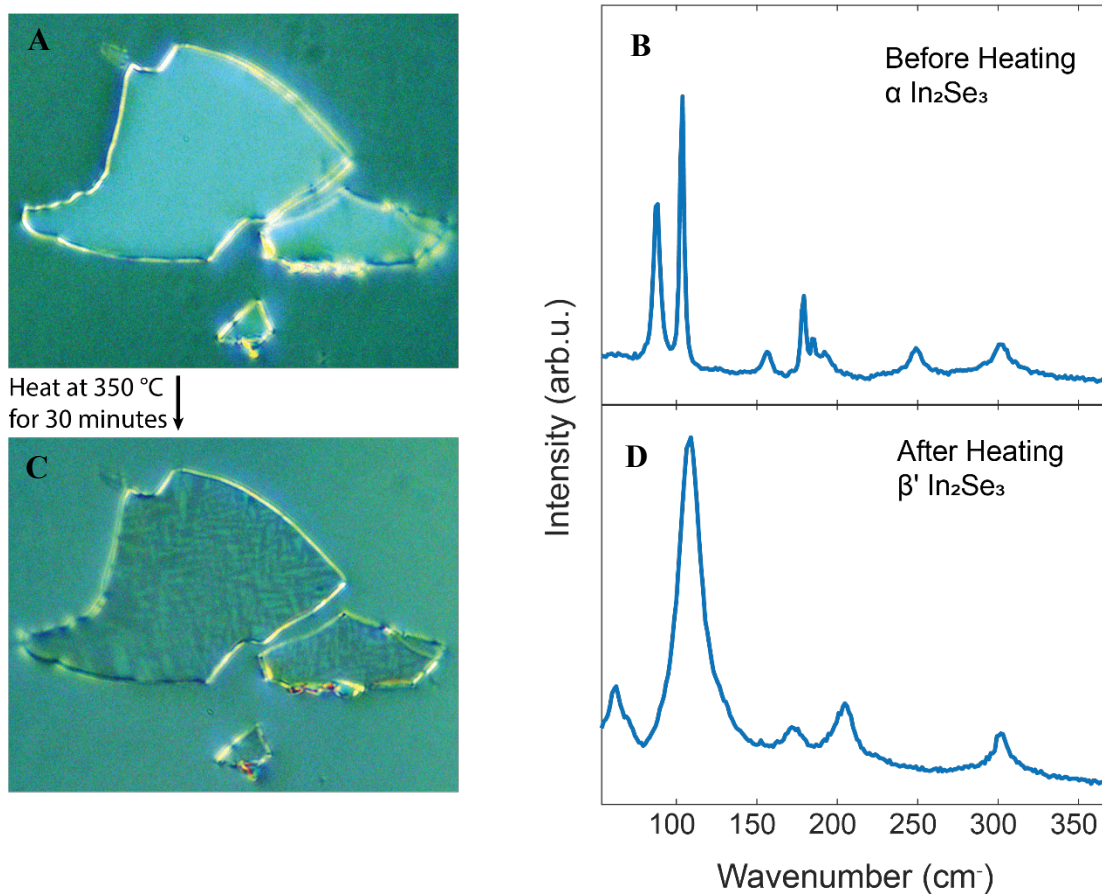


Fig. S1.

Phase change from α -In₂Se₃ to β' -In₂Se₃. (A) Cross polarized optical image of exfoliated In₂Se₃ flake before annealing does not show domain contrast and (B) Raman spectrum confirms this flake to be α phase. (C) Cross polarized optical image after annealing for 30 minutes at 350 °C. Domain contrast is present and (D) Raman spectrum confirms the flake is β' phase (47). All measurements were taken at room temperature and under ambient conditions.

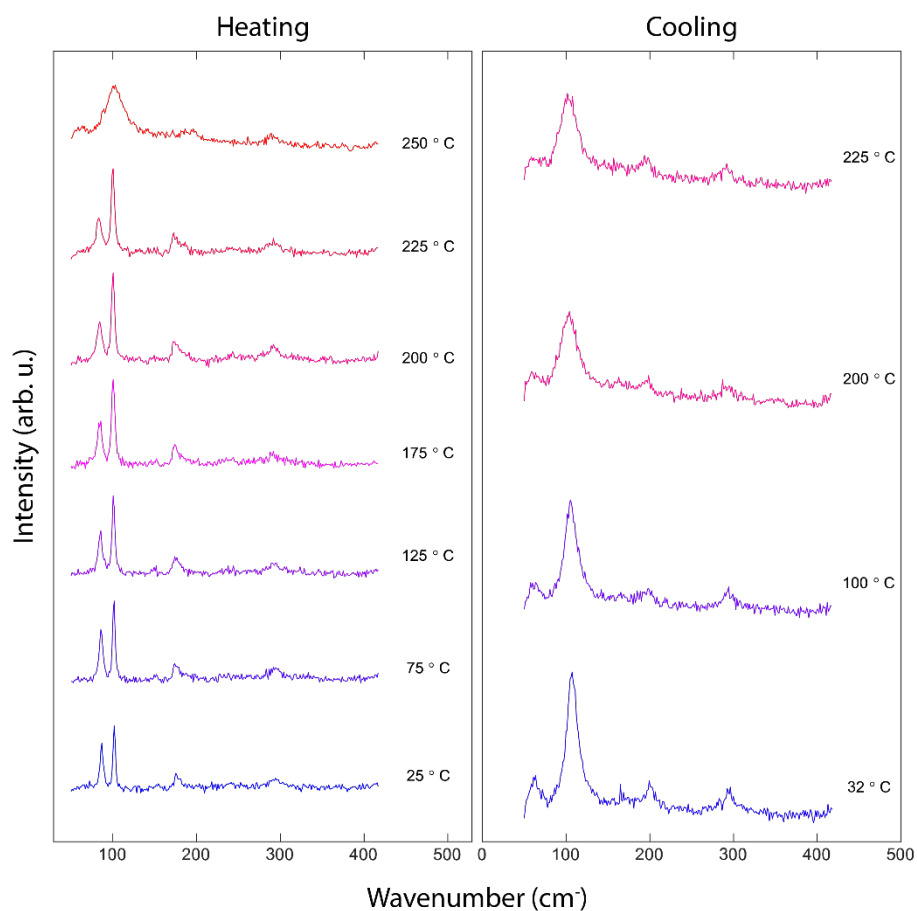


Fig. S2.

Temperature dependent Raman spectroscopy. Flake is initially α phase and converts to β phase between 225 °C and 250 °C. As the flake cools back to room temperature, it does not revert to the α phase, but relaxes to the β' phase. The α - β phase transition temperature is thickness dependent (16) and 200-250 °C was a typical value for flakes in this study. Heating to 350 °C as shown in Figure S1 was sufficient to convert most flakes on a particular sample.

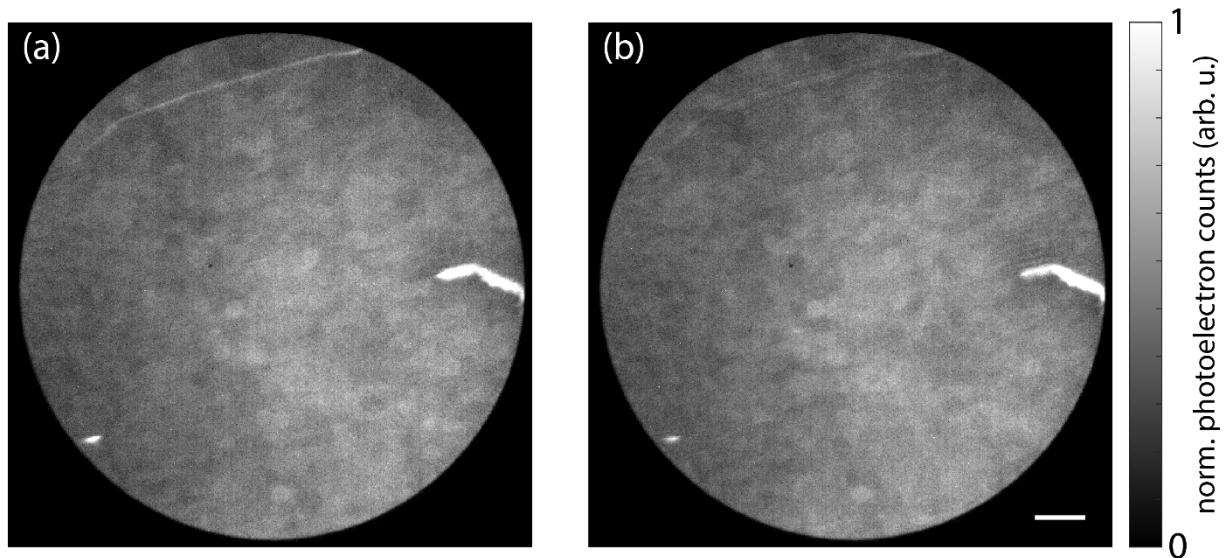


Fig. S3.

PEEM images of β' -In₂Se₃ with $h\nu = 3.1$ eV laser illumination polarized at (a) 50° and (b) 140° clockwise from the vertical axis. Contrast arises from differently oriented AFE domains. Scale bar: 3 μ m.

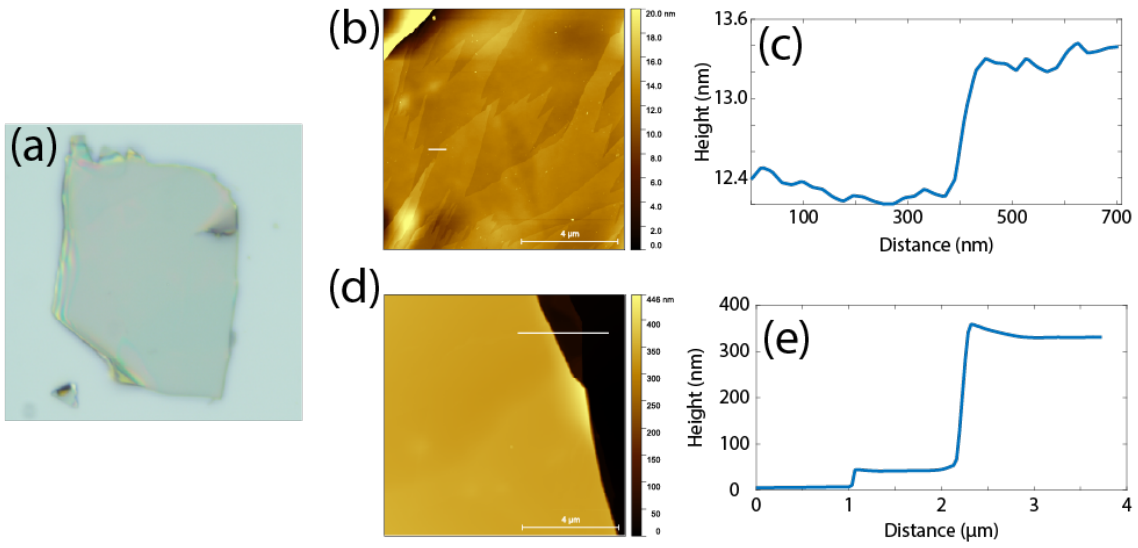


Fig. S4.

(a) Optical and (b,d) AFM images of the flake shown in Figures 1 and 5 of the main text. (c) Profile along AFM linecut shows that the flake surface is plane within single nanometer precision. There are monolayer terraces on the surface, but these do not correlate to domain boundaries. AFE domains are, therefore, not due to topographical features. (d) Profile along a line going over the edge of the flake shows the total thickness is about 330 nm.

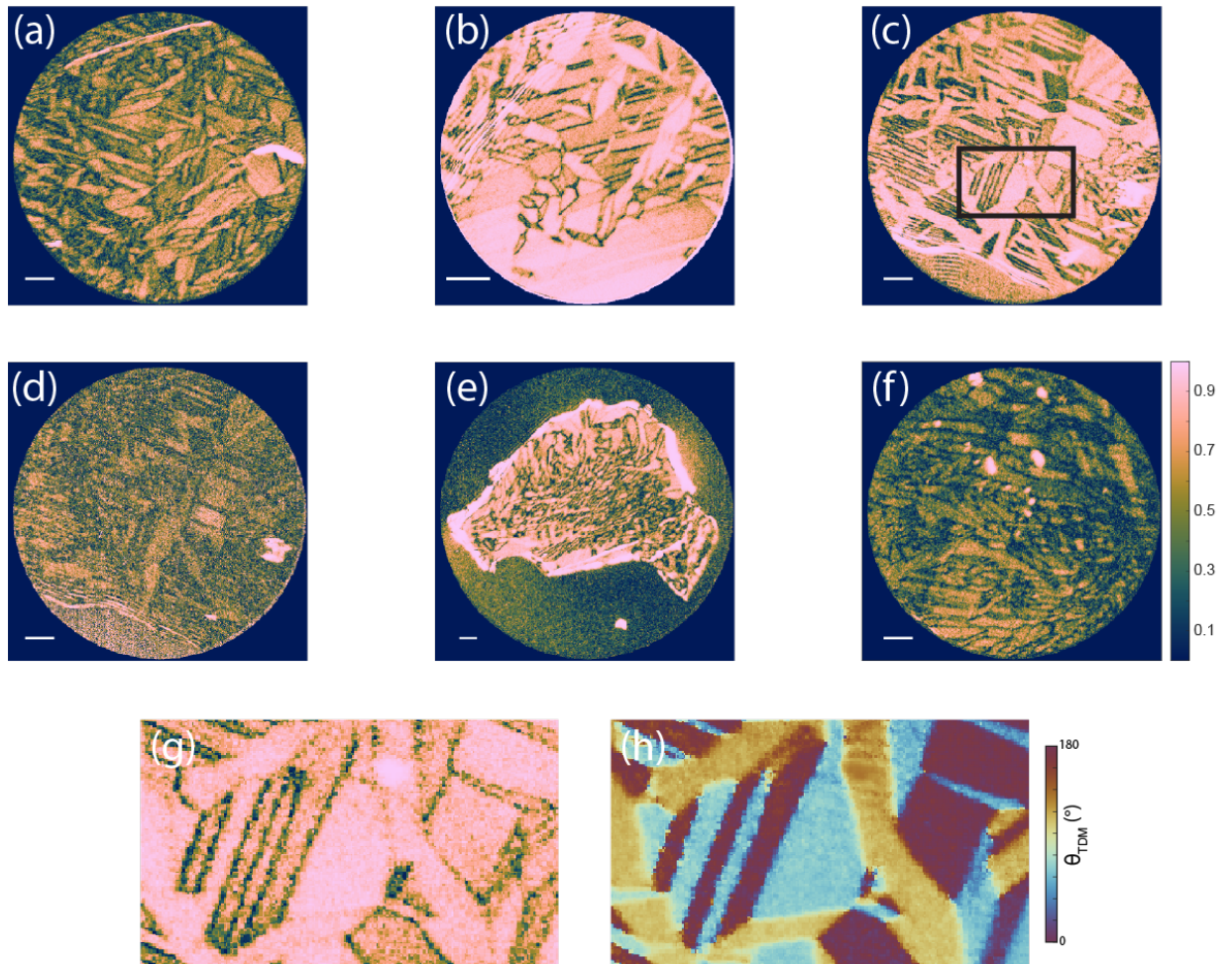


Fig. S5.

Maps of R^2 for pixel-by-pixel fitting of domains. (a) Figures 1, 5, S13, and S18(f); mean = 0.51. (b) Figures 2, S8, and S14(e); mean = 0.80. (c) Figures 4(a), S6(c), S9, and S19(a); mean = 0.73. (d) Figures 4(b) and S19(b); mean = 0.48. (e) Figure S14(a); mean = 0.50. (f) Figure S14(c); mean = 0.38. The region indicated in (c) is reproduced in (g) and shown in comparison to (h) a map of θ_{TDM} for the same region to verify that better fits do not correlate to a particular domain orientation. Scale bars: $3\mu\text{m}$.

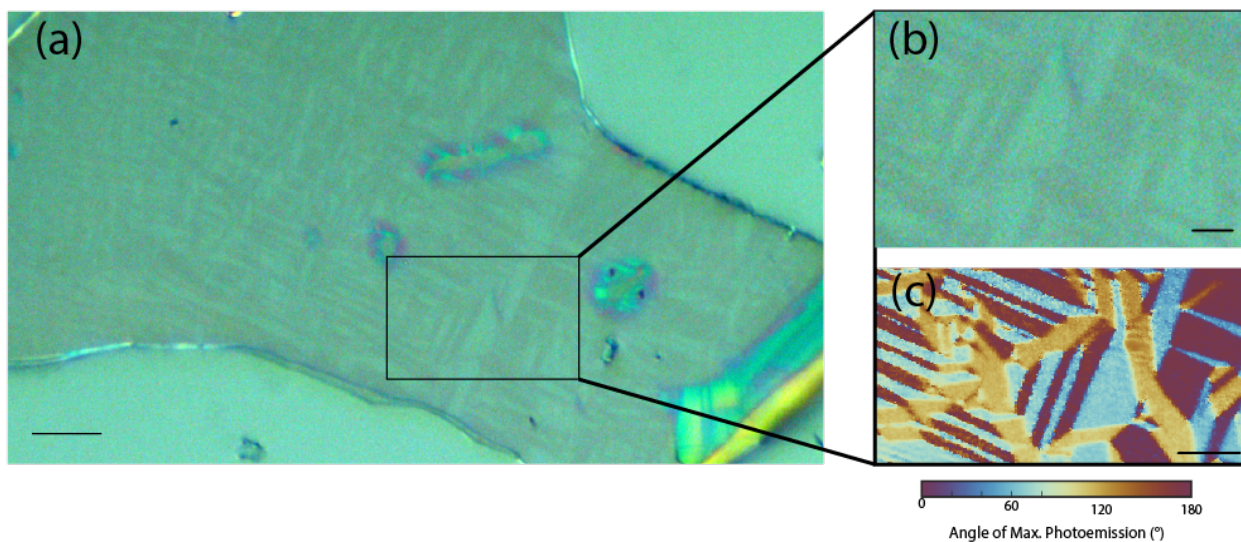


Fig. S6.

Domain visualization using (a,b) cross polarized optical microscopy (scale bars: $10\mu\text{m}$, $3\mu\text{m}$) and (c) PD-PEEM (3.06 eV excitation, scale bar: $3\mu\text{m}$) of the same region. Features not seen in the optical image are readily apparent in the PEEM data mapping.

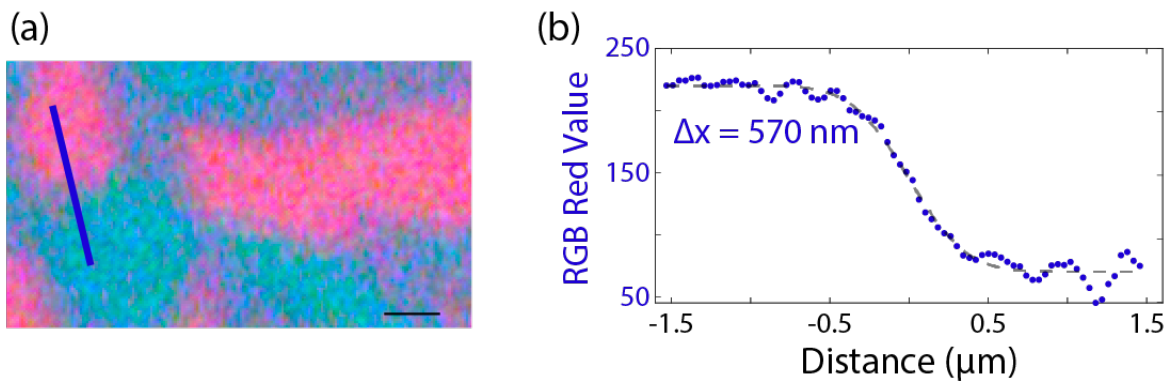


Fig. S7.

(a) Optical birefringence image of β' -In₂Se₃. (b) Resolution along the blue linecut in (a) where the fit is an error function and Δx is defined as the width between 16% and 84% the maximum. Scale bar: 1 μm .

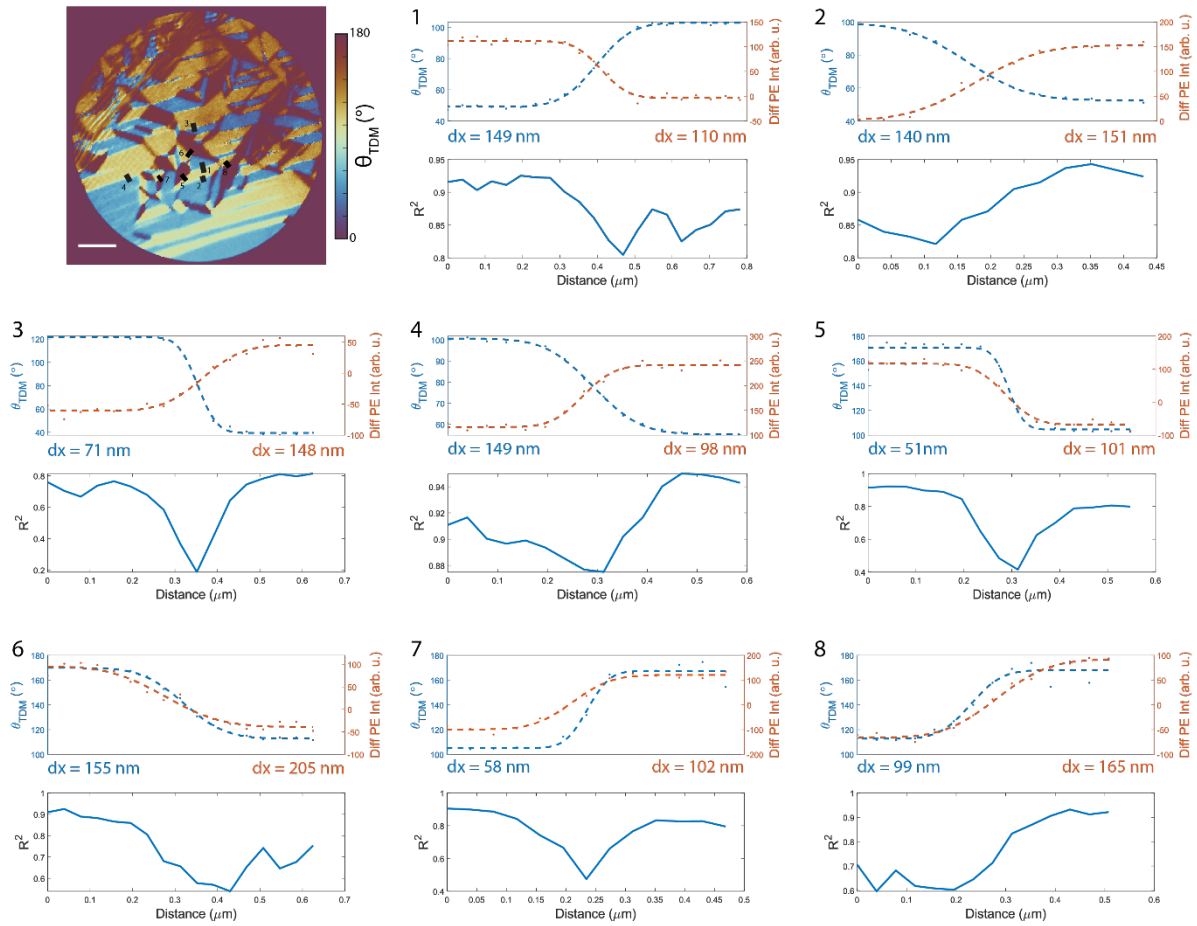


Fig. S8.

Resolution of β' -In₂Se₃ domains measured shown in Figure 2 of the main text. Values are along each of the linecuts shown in the θ_{TDM} map. Blue points are θ_{TDM} values and orange points are difference PE intensity; the R^2 value for each pixel along the linecut is shown below each trace. Fits are error functions and dx is defined as the width between 16% and 84% the maximum. Scale bar: 3 μm .

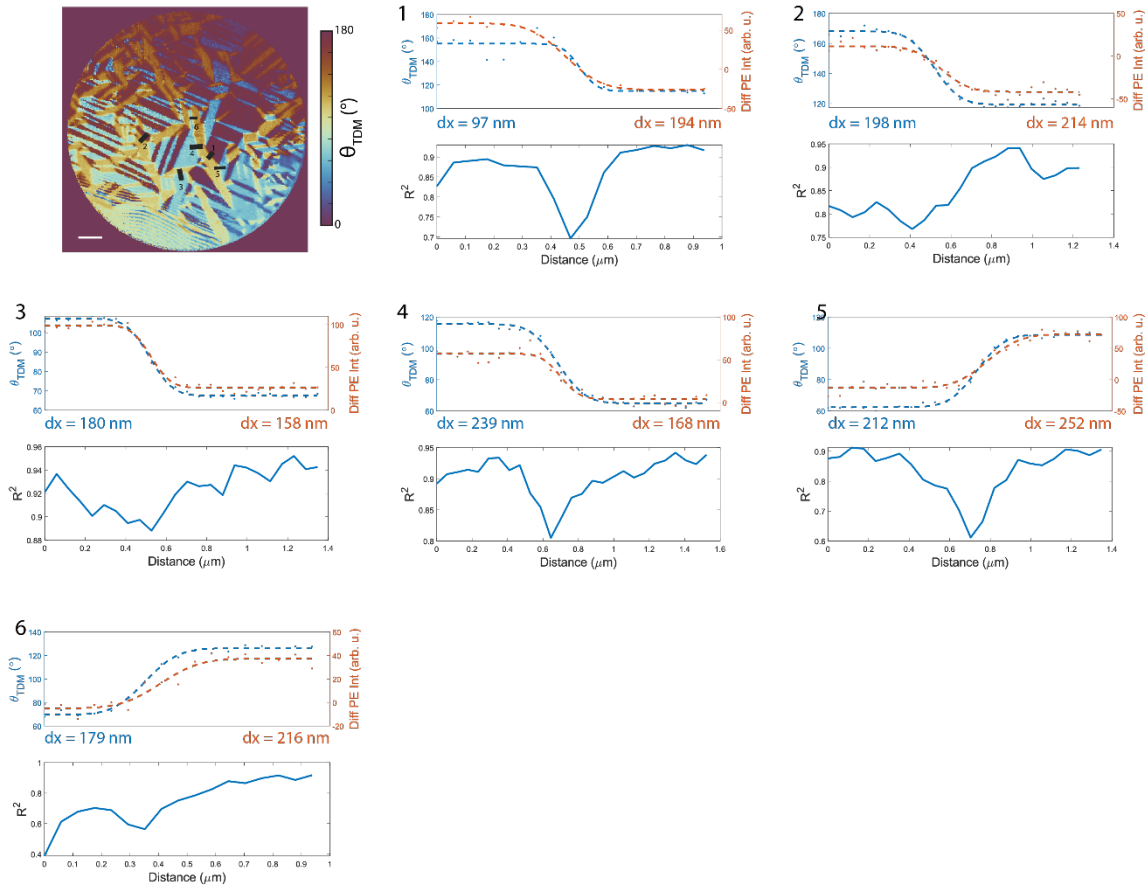


Fig. S9.

Resolution of β' -In₂Se₃ domains measured shown in Figure 4(a) of the main text. Values are along each of the linecuts shown in the θ_{TDM} map. Blue points are θ_{TDM} values and orange points are difference PE intensity; the R^2 value for each pixel along the linecut is shown below each trace. Fits are error functions and dx is defined as the width between 16% and 84% the maximum. Scale bar: $3\mu\text{m}$.

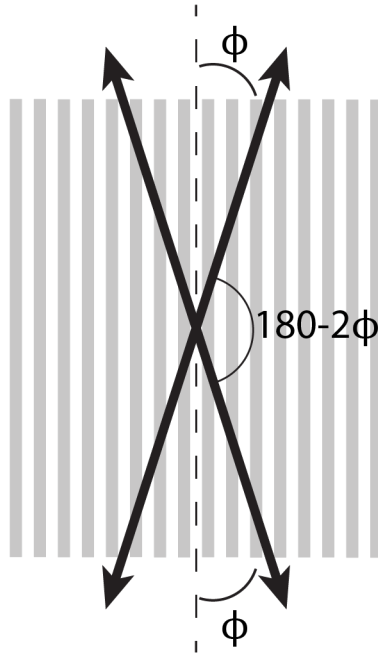


Fig. S10.

Symmetry consideration of transition dipole moment direction. Photoemission is maximized when the laser polarization is aligned with the transition dipole moment. If the transition dipole moment was rotated from the nanostructure direction by some value, ϕ , maxima would be separated by $180^\circ - 2\phi$ and 2ϕ rotations, due to the symmetry of the superstructure. Therefore, from the experimentally observed 180° periodicity we expect $\phi = 0$ or 90° . In other words, the transition dipole moment should be parallel or perpendicular to the nanostructure direction. A similar argument can be made for 180° periodicity in optical linear dichroism (48) and 90° periodicity in birefringence measurements (39,40).

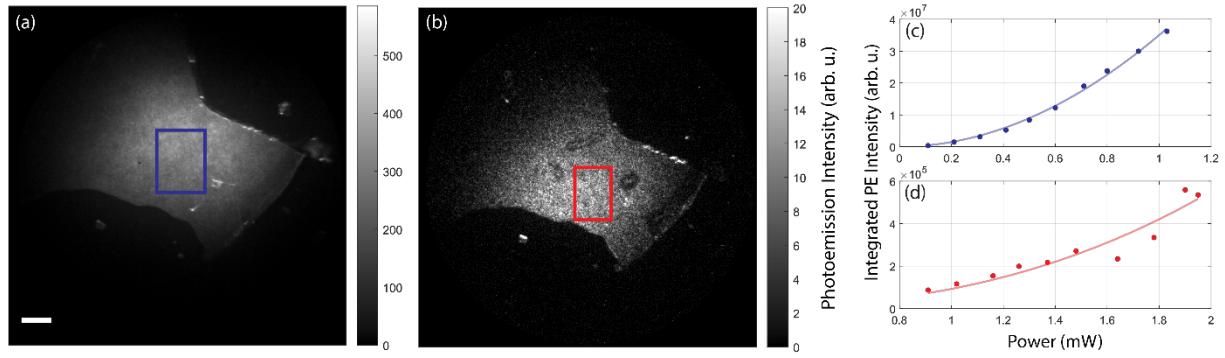


Fig. S11.

PEEM images of β' -In₂Se₃ flake imaged with (a) $h\nu = 3.06$ eV and (b) $h\nu = 2.40$ eV. Scalebar: 8 μ m. (c,d) Integrated PE intensity from the indicated regions vs illumination power. Dots are experimental values and solid lines are fits to $I = ax^b$. $b_{3.06 \text{ eV}} = 1.97$; $R^2_{3.06 \text{ eV}} = 0.996$. $b_{2.40 \text{ eV}} = 2.57$; $R^2_{2.40 \text{ eV}} = 0.902$.

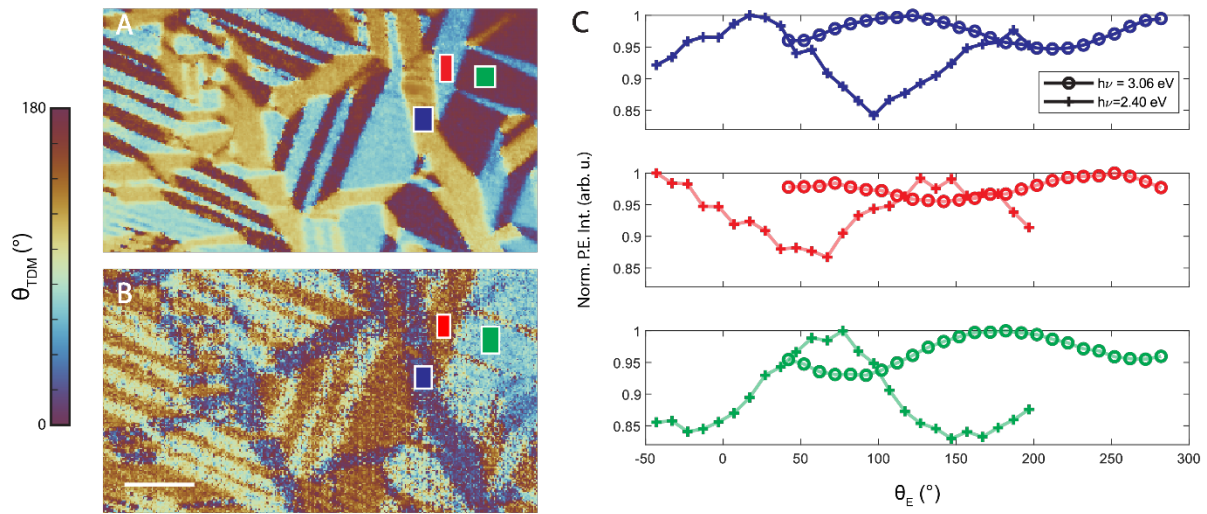


Fig. S12.

Maps of θ_{TDM} for a β' - In_2Se_3 flake imaged with (a) $h\nu = 3.06$ eV and (b) $h\nu = 2.40$ eV. (c) Integrated PE intensity from the indicated regions vs laser polarization. Scalebar: $3\ \mu\text{m}$.

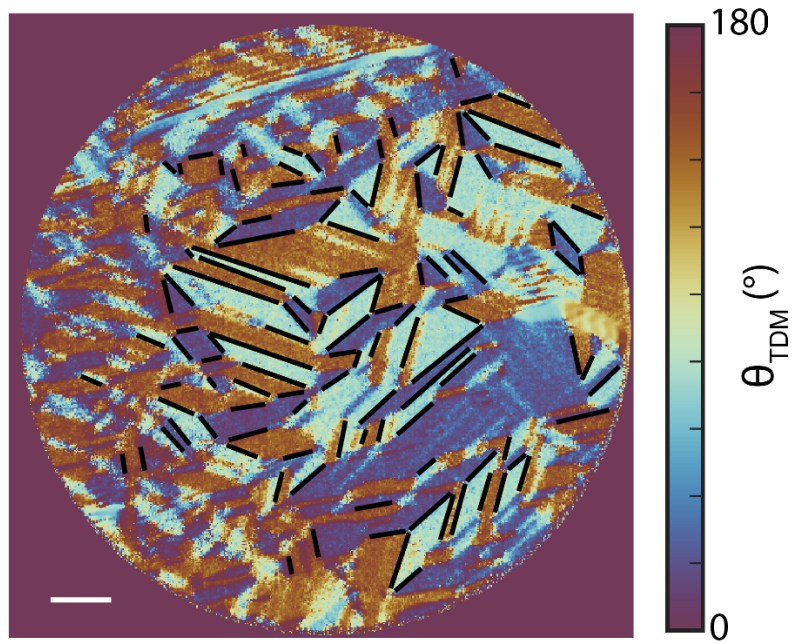


Fig. S13.

Domain walls measurement for the histogram shown in Figure 5 of the main text. In total, 120 domain boundaries were measured. Scale bar: $3\mu\text{m}$.

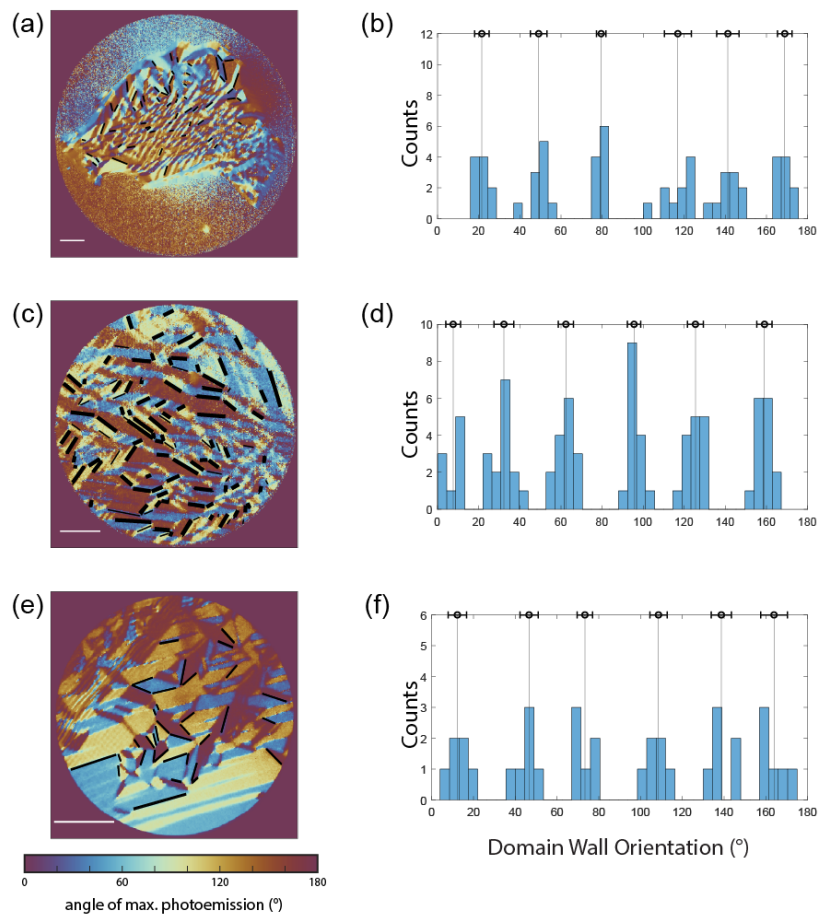


Fig. S14.

Domain walls analysis for additional flakes imaged with $h\nu = 3.1$ eV. $\sim 30^\circ$ difference between boundary orientations is consistent across all flakes. Scale bars: $5 \mu\text{m}$.

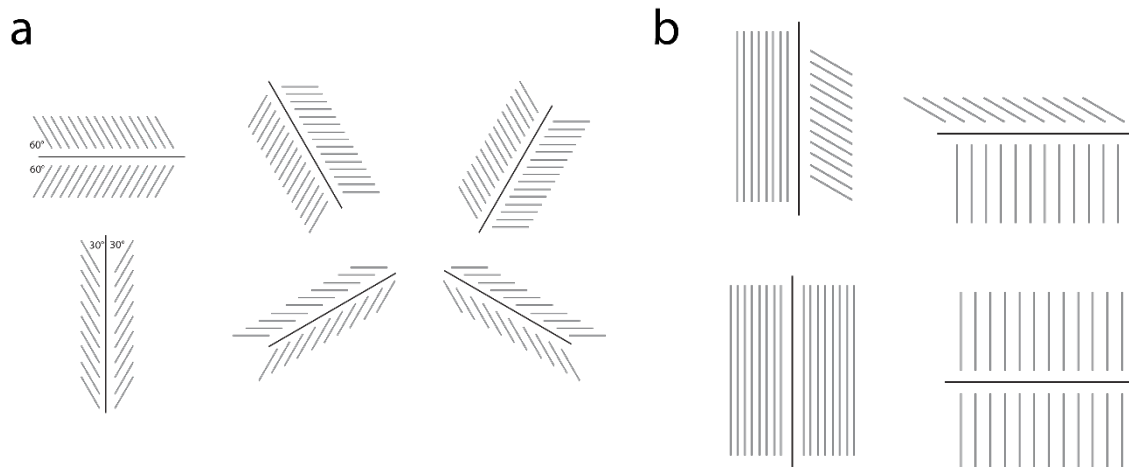


Fig. S15.

(a) Six possible domain boundary arrangements. Gray lines indicate nanostripes and black lines are boundaries. Nanostripes form 60° and 120° angles at $[\bar{1}100]$ and $[\bar{1}1\bar{2}0]$ boundaries, respectively. (b) Example of asymmetric 'forbidden' domain boundaries. Nanostripes cannot be parallel or perpendicular to a boundary that encloses their domain because this would result in either an asymmetric domain boundary or no change in orientation across the boundary (effectively no boundary).

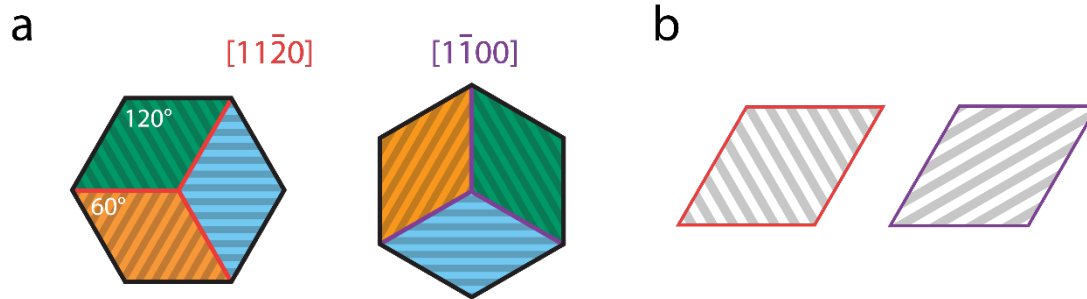


Fig. S16.

(a) The three possible orientations of the parallelograms for each set of vectors are colored green, blue, and orange. The shaded lines indicate the nanostripe direction. (b) If the lattice vectors orientations in a sample are not known the nanostripe direction for a particular domain cannot be uniquely determined from the shape analysis. Red and purple lines are $[11\bar{2}0]$ and $[1\bar{1}00]$ boundaries, respectively.

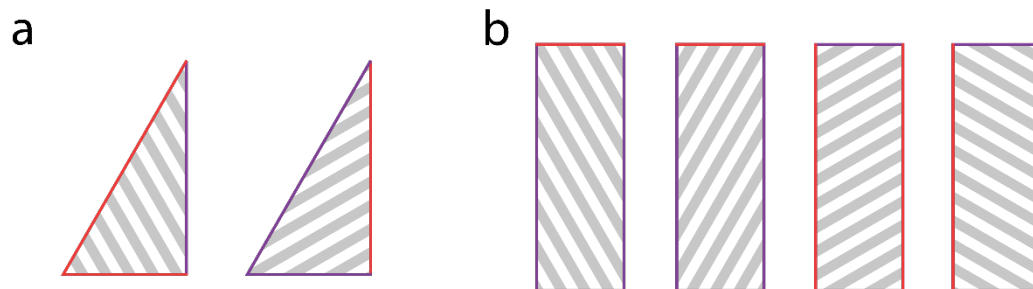


Fig. S17.

(a) Two possible nanostripe orientations in 30-60-90 right triangles. (a) Four possible nanostripe orientations in rectangular domains. Red and purple lines are $[11\bar{2}0]$ and $[1\bar{1}00]$ boundaries, respectively.

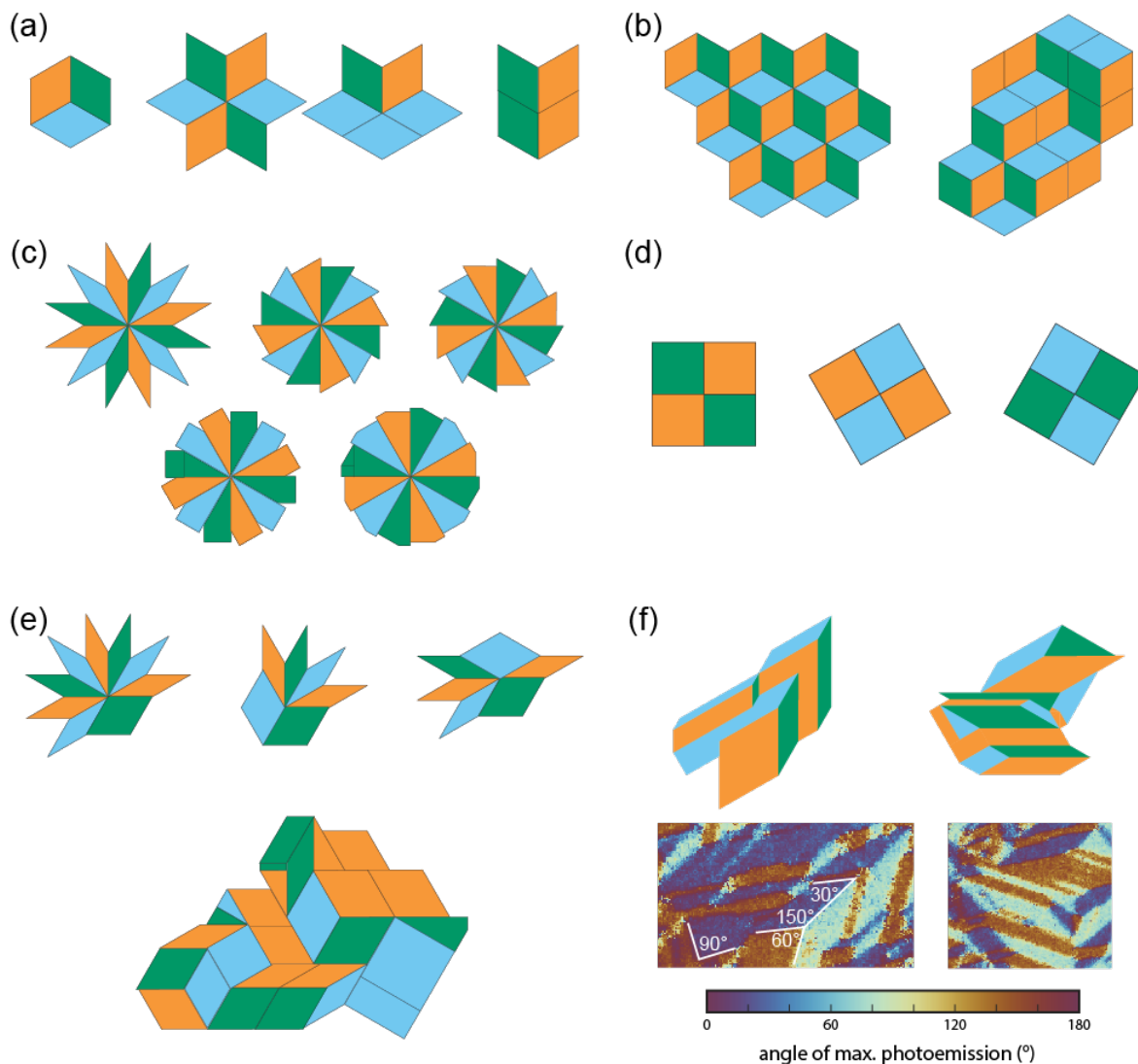


Fig. S18.

(a) All possible arrangements of domains if only one set of domain walls is used. Here, all domain walls are $[1\bar{1}00]$ in the coordinate system and color scheme defined in Figure S16(a). Equivalent patterns exist for the $[11\bar{2}0]$ domain walls that are simply rotated by 90° . The lines dividing regions of the same domain in the third and fourth pattern are not domain walls but illustrate how larger shapes may be composed of multiple 60-120 parallelograms. (b) Examples of patterns using the arrangements in (a). (c) Examples of domain shapes and arrangements when both sets of domain walls are used. (d) Arrangements of square domains. (e) Examples of complex and non-repeating patterns that are possible when both sets of domain walls are used. (f) Reconstruction of example patterns observed in PD-PEEM measurement.

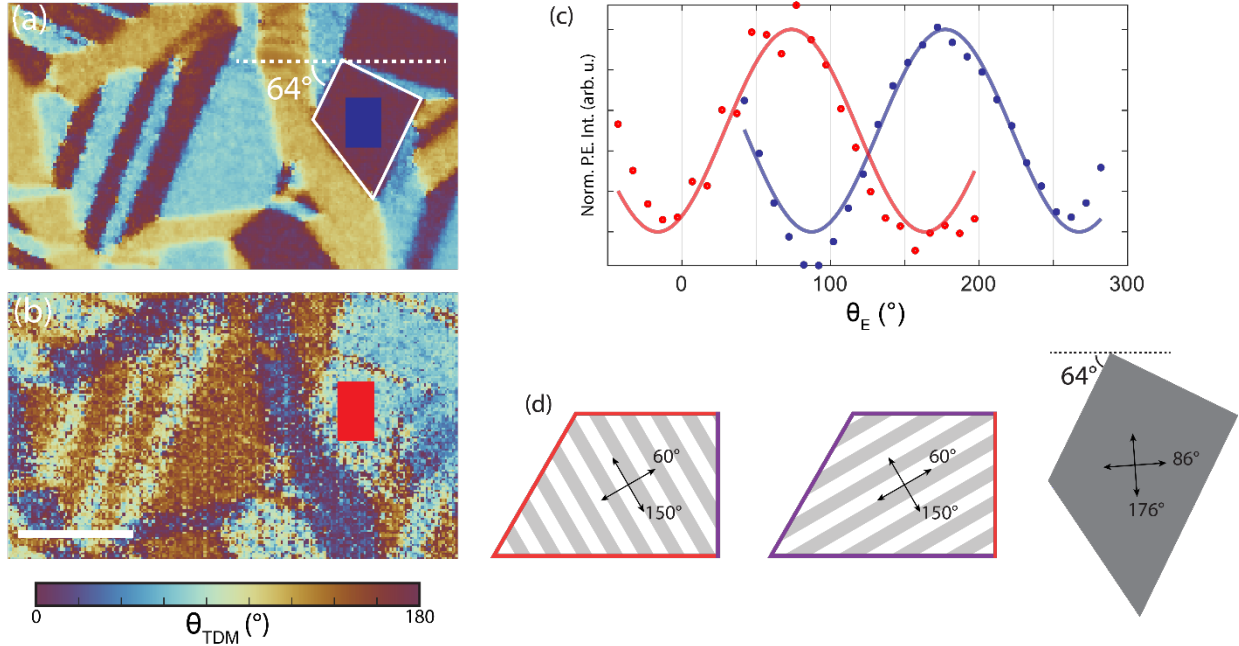


Fig. S19.

The expected orientation of nanostripes from the shape analysis are consistent with the PEEM data. For example, a 60-120-90-90 trapezoid was identified in the energy dependent experiments. A map of θ_{TDM} is shown for (a) 3.06 eV and (b) 2.40 eV excitation with red and blue ROIs, respectively, drawn on top of the trapezoids. The trapezoid is rotated 64° counterclockwise from the image horizontal, as depicted in (a). Scalebar: 3 μm . (c) Photoemission intensity vs polarization for each excitation energy shows a phaseshift between the two experiments. For the indicated ROIs, $\theta_{TDM}(3.06 \text{ eV}) = 177 \pm 3^\circ$ and $\theta_{TDM}(2.40 \text{ eV}) = 74 \pm 5^\circ$. Traces are normalized. (d) For this shape, there are two possible orientations of nanostripes, depending on where boundaries originates from each set of lattice vectors (indicated by orange and purple border shading). For both nanostripe directions, the parallel and perpendicular axes are at 60° and 150° so it is impossible to distinguish between these with optical measurements; it is only possible to identify the two orthogonal axes. For a trapezoid rotated by 64°, the axes are at 86° and 176°, in good agreement with the experimental measurement of θ_{TDM} . We attribute the $\sim 10^\circ$ deviation in the value recorded with $h\nu = 2.40 \text{ eV}$ to the lower SNR of that measurement.

Table S1. Comparison of Experimental Techniques for AFE domain imaging.

Technique	Field of View	Resolution	Requires UHV	Notes
PD-PEEM	10s of μm	<100 nm	✓	<ul style="list-style-type: none"> • Probes anisotropy of electronic transitions • Compatible with ultrafast spectroscopy • Unique resolution of domains • Flexible sample mounting and modulation • Requires conductive substrate
Optical Birefringence	100s of μm	100s of nm		<ul style="list-style-type: none"> • Probes anisotropy of electronic transitions • Compatible with ultrafast spectroscopy • Flexible sample mounting and modulation • Few restrictions on sample environment • Reduced periodicity in polarization response limits ability to distinguish different domains
Optical Transmission Microscopy	100s of μm	100s of nm		<ul style="list-style-type: none"> • Probes anisotropy of electronic transitions • Compatible with ultrafast spectroscopy • Few restrictions on sample environment • Requires optically transmissive substrates
STEM/4D-STEM	~ 100 nm (49)	Atomic	✓	<ul style="list-style-type: none"> • Structural imaging of atomic positions • Requires mounting samples on TEM grids • Ultrafast spectroscopy is very challenging
STM	~ 50 nm (50)	Atomic		<ul style="list-style-type: none"> • Convolution of atomic and electronic domain contrast • Sensitive to environment temperature (51) • Extremely surface sensitive • Ultrafast spectroscopy is not yet widely accessible (52)
PFM	10s of μm (7)	<10 nm (53)		<ul style="list-style-type: none"> • Probes amplitude and direction of piezoresponse • AFE domain contrast frequently not possible (7)

Movie S1.

Supplemental Movie 1 (In2Se3Movie.mp4): Movie of the difference PD-PEEM images corresponding to the map of θ_{TDM} shown in Figure 1 of the main text. Each frame is the difference in photoemission intensity at the indicated values of θ_{E} corrected for the Rh mirror reflectivity. Field of view is 30 μm and $h\nu = 3.1$ eV.

REFERENCES AND NOTES

1. Z. Liu, T. Lu, J. Ye, G. Wang, X. Dong, R. Withers, Y. Liu, Antiferroelectrics for energy storage applications: A review. *Adv. Mater. Technol.* **3**, 111 (2018).
2. C. A. Randall, Z. Fan, I. Reaney, L. Chen, S. Trolier-McKinstry, Antiferroelectrics: History, fundamentals, crystal chemistry, crystal structures, size effects, and applications. *J. Am. Ceram. Soc.* **104**, 3775–3810 (2021).
3. C. W. Ahn, G. Amarsanaa, S. S. Won, S. A. Chae, D. S. Lee, I. W. Kim, Antiferroelectric thin-film capacitors with high energy-storage densities, low energy losses, and fast discharge times. *ACS Appl. Mater. Interfaces* **7**, 26381–26386 (2015).
4. M. M. Vopson, X. Tan, Four-state anti-ferroelectric random access memory. *IEEE Electron Device Lett.* **37**, 1551–1554 (2016).
5. L. Liu, Y. Cai, X. Chen, Z. Liu, G. Yuan, Y. Wang, Flexible multi-state nonvolatile antiferroelectric memory. *J. Am. Ceram. Soc.* **105**, 6232–6240 (2022).
6. A. K. Tagantsev, K. Vaideswaran, S. B. Vakhrushev, A. V. Filimonov, R. G. Burkovsky, A. Shaganov, D. Andronikova, A. I. Rudskoy, A. Q. R. Baron, H. Uchiyama, D. Chernyshov, A. Bosak, Z. Ujma, K. Roleder, A. Majchrowski, J.-H. Ko, N. Setter, The origin of antiferroelectricity in PbZrO₃. *Nat. Commun.* **4**, 2229 (2013).
7. C. Xu, J. Mao, X. Guo, S. Yan, Y. Chen, T. W. Lo, C. Chen, D. Lei, X. Luo, J. Hao, C. Zheng, Y. Zhu, Two-dimensional ferroelasticity in van der Waals β' -In₂Se₃. *Nat. Commun.* **12**, 3665 (2021).
8. Q. N. Chen, Y. Ou, F. Ma, J. Li, Mechanisms of electromechanical coupling in strain based scanning probe microscopy. *Appl. Phys. Lett.* **104**, 242907 (2014).

9. Y. Kim, A. Kumar, A. Tselev, I. I. Kravchenko, H. Han, I. Vrejoiu, W. Lee, D. Hesse, M. Alexe, S. V. Kalinin, S. Jesse, Nonlinear phenomena in multiferroic nanocapacitors: Joule heating and electromechanical effects. *ACS Nano* **5**, 9104–9112 (2011).
10. A. K. Tagantsev, L. E. C. Cross, J. Fousek, *Domains in Ferroic Crystals and Thin Films* (Springer, 2010).
11. J. E. F. Gonzales, A. Ganzha, M. Kniazeva, D. Andronikova, A. Vakulenko, A. Filimonov, A. Rudskoy, C. Richter, A. Dasgupta, R. Gao, R. Burkovsky, Thickness independence of antiferroelectric domain characteristic sizes in epitaxial PbZrO₃/SrRuO₃/SrTiO₃ films. *J. Appl. Cryst.* **56**, 697–706 (2023).
12. B. Guzelturk, A. B. Mei, L. Zhang, L. Z. Tan, P. Donahue, A. G. Singh, D. G. Schlom, L. W. Martin, A. M. Lindenberg, Light-induced currents at domain walls in multiferroic BiFeO₃. *Nano Lett.* **20**, 145–151 (2020).
13. J. van Landuyt, G. van Tendeloo, S. Amelinckx, Phase transitions in In₂Se₃ as studied by electron microscopy and electron diffraction. *Phys. Status Solidi A* **30**, 299–314 (1975).
14. C. Manolikas, New results on the phase transformations of In₂Se₃. *J. Solid State Chem.* **74**, 319–328 (1988).
15. C. Zheng, L. Yu, L. Zhu, J. L. Collins, D. Kim, Y. Lou, C. Xu, M. Li, Z. Wei, Y. Zhang, M. T. Edmonds, S. Li, J. Seidel, Y. Zhu, J. Z. Liu, W.-X. Tang, M. S. Fuhrer, Room temperature in-plane ferroelectricity in van der Waals In₂Se₃. *Sci. Adv.* **4**, eaar7720 (2018).
16. X. Tao, Y. Gu, Crystalline-crystalline phase transformation in two-dimensional In₂Se₃ thin layers. *Nano Lett.* **13**, 3501–3505 (2013).

17. X. Zheng, W. Han, K. Yang, L. W. Wong, C. S. Tsang, K. H. Lai, F. Zheng, T. Yang, S. P. Lau, T. H. Ly, M. Yang, J. Zhao, Phase and polarization modulation in two-dimensional In₂Se₃ via in situ transmission electron microscopy. *Sci. Adv.* **8**, eabo0773 (2022).
18. W. Han, X. Zheng, K. Yang, C. S. Tsang, F. Zheng, L. W. Wong, K. H. Lai, T. Yang, Q. Wei, M. Li, W. F. Io, F. Guo, Y. Cai, N. Wang, J. Hao, S. P. Lau, C.-S. Lee, T. H. Ly, M. Yang, J. Zhao, Phase-controllable large-area two-dimensional In₂Se₃ and ferroelectric heterophase junction. *Nat. Nanotechnol.* **18**, 55–63 (2023).
19. S. Wan, Q. Peng, Z. Wu, Y. Zhou, Nonvolatile ferroelectric memory with lateral $\beta/\alpha/\beta$ In₂Se₃ heterojunctions. *ACS Appl. Mater. Interfaces* **14**, 25693–25700 (2022).
20. C. Xu, Y. Chen, X. Cai, A. Meingast, X. Guo, F. Wang, Z. Lin, T. W. Lo, C. Maunders, S. Lazar, N. Wang, D. Lei, Y. Chai, T. Zhai, X. Luo, Y. Zhu, Two-dimensional antiferroelectricity in nanostripe-ordered In₂Se₃. *Phys. Rev. Lett.* **125**, 047601 (2020).
21. J. L. Collins, C. Wang, A. Tadich, Y. Yin, C. Zheng, J. Hellerstedt, A. Grubišić-Čabo, S. Tang, S.-K. Mo, J. Riley, E. Huwald, N. V. Medhekar, M. S. Fuhrer, M. T. Edmonds, Electronic band structure of in-plane ferroelectric van der Waals β' -In₂Se₃. *ACS Appl. Electron. Mater.* **2**, 213–219 (2020).
22. F. Zhang, Z. Wang, J. Dong, A. Nie, J. Xiang, W. Zhu, Z. Liu, C. Tao, Atomic-scale observation of reversible thermally driven phase transformation in 2D In₂Se₃. *ACS Nano* **13**, 8004–8011 (2019).
23. Z. Zhang, J. Nie, Z. Zhang, Y. Yuan, Y. Fu, W. Zhang, Atomic visualization and switching of ferroelectric order in β -In₂Se₃ films at the single layer limit. *Adv. Mater.* **34**, e2106951 (2022).

24. J. Schaab, I. P. Krug, F. Nickel, D. M. Gottlob, H. Döganay, A. Cano, M. Hentschel, Z. Yan, E. Bourret, C. M. Schneider, R. Ramesh, D. Meier, Imaging and characterization of conducting ferroelectric domain walls by photoemission electron microscopy. *Appl. Phys. Lett.* **104**, 232904 (2014).
25. N. Barrett, J. E. Rault, J. L. Wang, C. Mathieu, A. Locatelli, T. O. Mentès, M. A. Niño, S. Fusil, M. Bibes, A. Barthélemy, D. Sando, W. Ren, S. Prosandeev, L. Bellaiche, B. Vilquin, A. Petraru, I. P. Krug, C. M. Schneider, Full field electron spectromicroscopy applied to ferroelectric materials. *J. Appl. Phys.* **113**, 187217 (2013).
26. J. E. Rault, W. Ren, S. Prosandeev, S. Lisenkov, D. Sando, S. Fusil, M. Bibes, A. Barthélemy, L. Bellaiche, N. Barrett, Thickness-dependent polarization of strained BiFeO₃ films with constant tetragonality. *Phys. Rev. Lett.* **109**, 267601 (2012).
27. M. Ghidini, F. Maccherozzi, S. S. Dhési, N. D. Mathur, XPEEM and MFM imaging of ferroic materials. *Adv. Electron. Mater.* **8**, 162 (2022).
28. A. Sander, M. Christl, C.-T. Chiang, M. Alexe, W. Widdra, Domain imaging on multiferroic BiFeO₃(001) by linear and circular dichroism in threshold photoemission. *J. Appl. Phys.* **118**, 224102 (2015).
29. J. M. Frost, K. T. Butler, F. Brivio, C. H. Hendon, M. van Schilfgaarde, A. Walsh, Atomistic origins of high-performance in hybrid halide perovskite solar cells. *Nano Lett.* **14**, 2584–2590 (2014).
30. X. Xiao, W. Li, Y. Fang, Y. Liu, Y. Shao, S. Yang, J. Zhao, X. Dai, R. Zia, J. Huang, Benign ferroelastic twin boundaries in halide perovskites for charge carrier transport and recombination. *Nat. Commun.* **11**, 2215 (2020).

31. X.-K. Wei, T. Sluka, B. Fraygola, L. Feigl, H. Du, L. Jin, C.-L. Jia, N. Setter, Controlled charging of ferroelastic domain walls in oxide ferroelectrics. *ACS Appl. Mater. Interfaces* **9**, 6539–6546 (2017).
32. P. P. Joshi, R. Li, J. L. Spellberg, L. Liang, S. B. King, Nanoimaging of the edge-dependent optical polarization anisotropy of black phosphorus. *Nano Lett.* **22**, 3180–3186 (2022).
33. A. Neff, F. Niefind, B. Abel, S. C. B. Mannsfeld, K. R. Siefermann, Imaging nanoscale morphology of semiconducting polymer films with photoemission electron microscopy. *Adv. Mater.* **29**, 1701012 (2017).
34. F. Cramer, G. E. Shephard, P. J. Heron, The misuse of colour in science communication. *Nat. Commun.* **11**, 5444 (2020).
35. F. Cramer, Scientific colour maps, version 8.0.1, Zenodo (2023); <https://doi.org/10.5281/zenodo.8409685>.
36. M. Aeschlimann, M. Bauer, D. Bayer, T. Brixner, F. J. G. de Abajo, W. Pfeiffer, M. Rohmer, C. Spindler, F. Steeb, Adaptive subwavelength control of nano-optical fields. *Nature* **446**, 301–304 (2007).
37. M. Dabrowski, Y. Dai, H. Petek, Ultrafast microscopy: Imaging light with photoelectrons on the nano-femto scale. *J. Phys. Chem. Lett.* **8**, 4446–4455 (2017).
38. M. K. L. Man, A. Margiolakis, S. Deckoff-Jones, T. Harada, E. L. Wong, M. B. M. Krishna, J. Madéo, A. Winchester, S. Lei, R. Vajtai, P. M. Ajayan, K. M. Dani, Imaging the motion of electrons across semiconductor heterojunctions. *Nat. Nanotechnol.* **12**, 36–40 (2017).
39. M. Sabooni, A. N. Nilsson, G. Kristensson, L. Rippe, Wave propagation in birefringent materials with off-axis absorption or gain. *Phys. Rev. A* **93**, 013842 (2016).
40. S. Haussühl, *Physical Properties of Crystals* (Wiley-VCH, 2007).

41. A. Castellanos-Gomez, M. Buscema, R. Molenaar, V. Singh, L. Janssen, H. S. J. van der Zant, G. A. Steele, Deterministic transfer of two-dimensional materials by all-dry viscoelastic stamping. *2D Mater.* **1**, 011002 (2014).
42. G. Kresse, J. Furthmüller, Efficient iterative schemes for ab initio total-energy calculations using a plane-wave basis set. *Phys. Rev. B* **54**, 11169–11186 (1996).
43. G. Kresse, D. Joubert, From ultrasoft pseudopotentials to the projector augmented-wave method. *Phys. Rev. B* **59**, 1758–1775 (1999).
44. J. P. Perdew, K. Burke, M. Ernzerhof, Generalized gradient approximation made simple. *Phys. Rev. Lett.* **77**, 3865–3868 (1996).
45. J. H. Weaver, C. G. Olson, D. W. Lynch, Optical investigation of the electronic structure of bulk Rh and Ir. *Phys. Rev. B* **15**, 4115–4118 (1977).
46. X. Ling, S. Huang, E. H. Hasdeo, L. Liang, W. M. Parkin, Y. Tatsumi, A. R. T. Nugraha, A. A. Puretzky, P. M. Das, B. G. Sumpter, D. B. Geohegan, J. Kong, R. Saito, M. Drndic, V. Meunier, M. S. Dresselhaus, Anisotropic electron-photon and electron-phonon interactions in black phosphorus. *Nano Lett.* **16**, 2260–2267 (2016).
47. F. Lyu, X. Li, J. Tian, Z. Li, B. Liu, Q. Chen, Temperature-driven α - β phase transformation and enhanced electronic property of 2H α -In₂Se₃. *ACS Appl. Mater. Interfaces* **14**, 23637–23644 (2022).
48. A. Rodger, B. Nordén, Circular Dichroism and Linear Dichroism (Oxford Univ. Press, 1997).
49. N. Shibata, Y. Kohno, A. Nakamura, S. Morishita, T. Seki, A. Kumamoto, H. Sawada, T. Matsumoto, S. D. Findlay, Y. Ikuhara, Atomic resolution electron microscopy in a magnetic field free environment. *Nat. Commun.* **10**, 2308 (2019).

50. L. Jones, S. Wang, X. Hu, S. Ur Rahman, M. R. Castell, Maximising the resolving power of the scanning tunneling microscope. *Adv. Struct. Chem. Imaging* **4**, 7 (2018).
51. T. Esat, X. Yang, F. Mustafayev, H. Soltner, F. S. Tautz, R. Temirov, Determining the temperature of a millikelvin scanning tunnelling microscope junction. *Commun. Phys.* **6**, 81 (2023).
52. K. Liang, L. Bi, Q. Zhu, H. Zhou, S. Li, Ultrafast dynamics revealed with time-resolved scanning tunneling microscopy: A review. *ACS Appl. Opt. Mater.* **1**, 924–938 (2023).
53. A. Gruverman, M. Alexe, D. Meier, Piezoresponse force microscopy and nanoferroic phenomena. *Nat. Commun.* **10**, 1661 (2019). Z:\scienceprod\sciadv\full\sciadv.ado2136\SM